Available online at www.HighTechJournal.org

HighTech and Innovation Journal

ISSN: 2723-9535

Vol. 5, No. 3, September, 2024

Innovative Metal Powder Production Using CFD with Convergent-Divergent Nozzles in Wire Arc Atomization

Matee Sukkee [1], Phanphong Kongphan [1*]

[1] Department of Industrial Engineering, Faculty of Engineering, Rajamangala University of Technology Thanyaburi, Pathum Thani 12110, Thailand.

Received 24 May 2024; Revised 19 August 2024; Accepted 25 August 2024; Published 01 September 2024

Abstract

This study aims to enhance the production of metal powders using a novel approach that integrates computational fluid dynamics (CFD) with convergent-divergent (C-D) nozzles in wire arc spraying atomization (WASA). The primary objective is to investigate the influence of nozzle design on particle size distribution and production efficiency. Utilizing the ANSYS CFD Fluent program, simulations were conducted to analyze the effects of various parameters, including throat diameter and divergent angles, on gas dynamics and metal droplet behavior. The findings reveal that C-D nozzles facilitate the acceleration of gas flow to supersonic speeds, significantly improving the shear force acting on the molten metal, thereby promoting the fragmentation of droplets into smaller particles. Notably, the optimized nozzle configuration achieved a median particle size (D_{50}) of 44.42 µm, suitable for additive manufacturing applications. The novelty of this work lies in its comprehensive simulation framework that allows for rapid virtual testing, potentially leading to significant improvements in the efficiency and quality of metal powder production processes. This research addresses critical gaps in the existing literature and provides a robust foundation for future studies in the field of metal powder manufacturing.

Keywords: Computational Fluid Dynamics; Convergent-Divergent Nozzles; Wire Arc Spraying Atomization; Metal Powder Manufacturing.

1. Introduction

The production of metal powder is a fundamental process to generate the raw materials for various industrial applications, including additive manufacturing, powder metallurgy [1, 2], and surface coating technologies [3]. Wire Arc Spraying Atomization (WASA) is a novel technique used to produce metal powders. This method involves the utilization of an electric arc to melted metal wire, followed by the dispersion of the melted metal through a high-speed gas stream. When the droplets cool down, they undergo a process of solidification and transform into small particles of metal powder [4-6]. The nozzle used to control the gas flow is a key element of this technique. The conventional nozzles commonly employed in wire arc spraying systems often face challenges in achieving a constant particle size distribution and maintaining maximum production efficiency. Several studies have been driven by the need for improved efficiency to generate several types of nozzles. A novel method involves utilizing convergent-divergent (C-D) nozzles [7, 8], which are originally designed for supersonic applications, such as rocket engines [9, 10]. The C-D nozzles operate by converging the gas flow to increase its velocity and then diverging to maintain a high speed over a longer distance. This facilitates the achievement of supersonic speeds, which is beneficial for the atomization process in wire arc spraying. Integrating C-D nozzles into wire arc spraying systems is a potentially beneficial yet challenging approach. Employing Computational Fluid Dynamics (CFD) for simulating complex gas flows and particle transformations within the nozzle

* Corresponding author: phanphong.k@en.rmutt.ac.th

http://dx.doi.org/10.28991/HIJ-2024-05-03-02

offers an efficient solution that preserves time and resources [11]. Moreover, computational simulation allows for the rapid execution of several virtual tests, which is sometimes not possible with physical testing.

The C-D nozzle plays a pivotal role in the atomization process of metals, as it accelerates gas flow to supersonic speeds in the divergent section, which is critical for generating the shear force needed to break metal droplets into finer particles. Early studies, such as those by Chen et al. [12], explored aspects like the arc spraying gun design, external gas flow configuration, and droplet atomization but did not provide a comprehensive analysis of the entire process. More recently, Malik et al. [13] investigated optimal convergence angles for C-D nozzles by assessing how changes in these angles influence flow parameters. Despite substantial research on convergence angles, there is still a significant gap regarding the influence of divergent angles on flow dynamics. Additionally, Khalid et al. [14] used computational fluid dynamics (CFD) to analyze compressible flow through converging nozzles, aiming to understand the impact of nozzle design on rocket performance, but they did not consider thermal effects or material properties. In a different study, Shuvo et al. [15] employed Eulerian-Lagrangian techniques to examine particle accumulation in the turbulent flow within C-D nozzles, though their research did not specifically target metal powder production. Similarly, Urionabarrenetxea et al. [16] used CFD to simulate gas flow in a close-coupled gas injector, but this study did not investigate a wide range of nozzle configurations for optimizing metal powder production. Kumar et al. [17] also utilized CFD to analyze how inlet and outlet angles affect flow characteristics in C-D nozzles designed for rocket motors, but their findings were not extended to industrial applications, particularly metal powder production. And Zema et al. [18] examined flow characteristics within C-D nozzles, highlighting the effects of geometric and operational parameters on variables such as velocity, pressure, and temperature across different nozzle sections. However, their research did not delve into the role of micro-jets in controlling flow within the nozzle.

Recently, Hua et al. [19] introduced a numerical modeling framework that accurately predicts how various parameters and material properties influence particle size distribution during gas atomization. Although this study focused on nickel-silicon alloys, it highlighted a gap in research on other materials. Similarly, Samuel et al. [20] utilized a CFD model of the Close-Coupled Gas Atomization (CCGA) process to examine the impact of the gas-to-melt ratio on atomization, shedding light on the fundamental physics of the melt-gas interaction. However, their work did not address the flow dynamics or the characteristics of the resulting particles. Wang et al. [21] advanced the understanding of droplet breakup mechanisms during gas atomization, though the secondary breakup of metal droplets remains a complex area, lacking a thorough description of these processes. Muratal et al. [22] explored how gas atomization parameters affect the production of Ni-Hard alloy powders, with a focus on improving particle size distribution and surface quality. However, their study was limited to specific parameters like gas pressure and did not cover a wider range of conditions. Cui et al. [23] examined gas atomization for duplex stainless steel powders, finding that optimized powder characteristics led to better density and mechanical properties in the final parts. Following this, Çetin et al. [24] studied the impact of gas pressure on AM60 magnesium alloy powders, discovering that higher gas pressure resulted in smaller powder sizes and a morphological shift from irregular shapes to more spherical forms. They emphasized a lack of research on the production and characterization of metal powders, calling for more in-depth studies to better understand their properties. Finally, Luo et al. [25] investigated fluid behavior during gas atomization, revealing that the physical properties of the liquid, such as viscosity and surface tension, are crucial in determining the breakup behavior. However, this research concentrated primarily on the properties of the produced powders, leaving a gap in understanding how fluid dynamics influence powder quality and size distribution.

The primary objective of this research is to address the gaps identified in previous studies by focusing on the simulation of the effects of nozzle shape variations in the C-D nozzle for the production of Ag925 precious metal powder. Past research on the metal powder production process using C-D nozzles has extensively examined the geometry and parameters impacting particle characteristics, such as gas pressure, type of gas, gas-to-metal ratio, melting temperature, and nozzle shape design; however, these aspects have not been comprehensively and clearly addressed. Moreover, the investigation of flow velocity and shock waves has been insufficiently explored for the production of Ag925 precious metal powder using wire arc atomization techniques, representing a significant gap that requires urgent attention. Consequently, this study aims to utilize CFD to simulate the flow of gas and molten metal within the C-D nozzle to investigate and analyze the impact of nozzle shape variations on the characteristics of Ag925 precious metal powder. The research will encompass an exploration of several key factors, including flow velocity, flow pressure, shock waves, and droplet temperature, which will provide critical data for the advancement of metal powder production technology in the future, particularly in industries that require fine and high-quality metal powders for additive manufacturing.

2. Research Methodology

The flowchart presents a systematic approach for modeling, validating, and simulating the TATF-400 and C-D nozzles using computational fluid dynamics (CFD) (Figure 1). The process begins with the creation of a detailed 3D model of the TATF-400 nozzle. Once the 3D model is finalized, the next step involves meshing the nozzle, preparing it for subsequent simulation. Following meshing, a grid independence verification is performed to ensure that the simulation results are not influenced by the mesh resolution. If the model fails this verification, necessary adjustments are made, and the process is repeated until grid independence is achieved. Once validated, boundary conditions and solver configurations specific to the TATF-400 nozzle are applied. The model then undergoes validation, in which the simulation results are compared against experimental data. If the results do not align with these benchmarks, adjustments are made to the model configuration, and the validation process is repeated. Upon successful validation of the TATF-400 model, attention shifts to the C-D nozzle.

The process for the C-D nozzle begins with meshing, followed by the application of boundary conditions and solver settings tailored to this nozzle's specific requirements. Once the necessary parameters have been configured, simulations for the C-D nozzle are carried out, and the results are analyzed. Finally, conclusions are drawn based on the outcomes of the simulations, marking the end of the procedure.

This rigorous and structured methodology ensures a thorough and reliable analysis of both the TATF-400 and C-D nozzles, enabling accurate and robust CFD simulations.

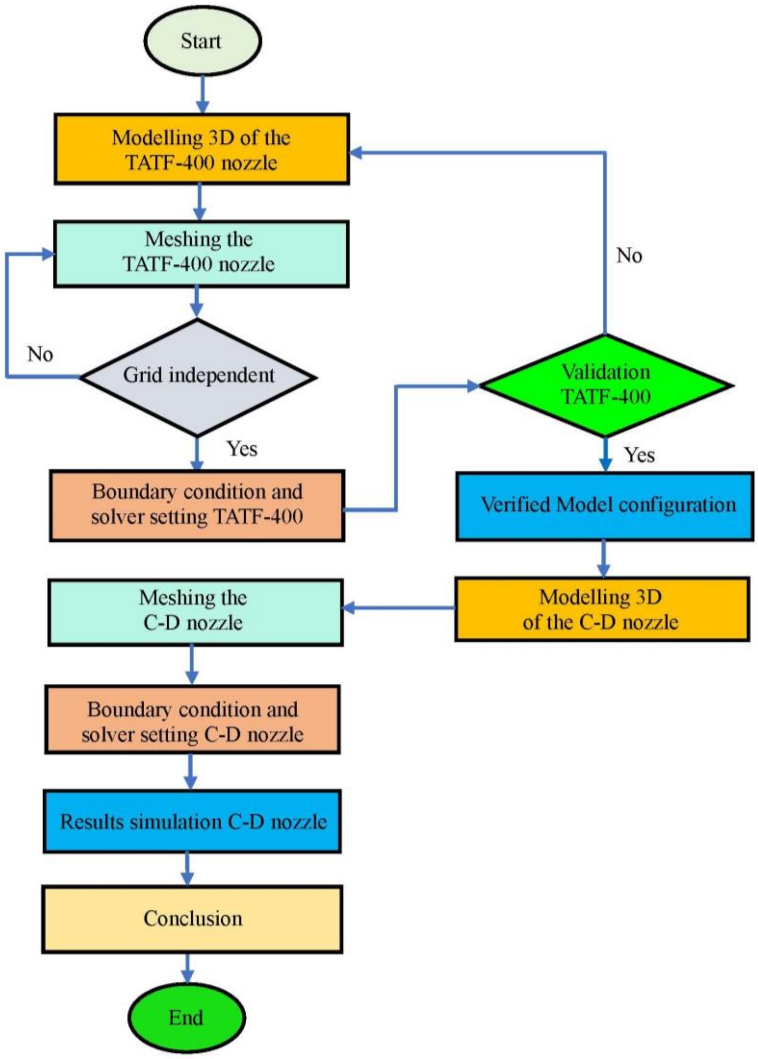

Figure 1. Flowchart of the methodology

2.1. Modeling 3D Configuration

Figure 2a shows the TATF-400 nozzle, which has been specifically designed for metal coating applications. The nozzle has a converging shape with a 30-degree angle. The gas inlet has a diameter of 10 mm, and the wire arc angle is 28 degrees. According to previous research, the TATF-400 nozzle was tested for metal powder production using the wire arc spraying technique. The experiment yielded results on the particle size distribution of the metal powder. These experimental results will be compared with the simulation results of this model. Subsequently, the model used to simulate the TATF-400 nozzle will be applied to simulate the C-D nozzle, as shown in Figure 2b. Based on the shape of the C-D nozzle, it can be observed that the converging angle is larger than the diverging angle, which results in higher values for Mach number, static pressure, and turbulent intensity compared to nozzle designs where the converging angle is smaller than the diverging angle [26-29]. It is widely accepted that a diverging angle of approximately 6°~7° (half of the total angle) contributes to an optimal balance between nozzle length and the likelihood of boundary layer separation, while also minimizing energy losses [30]. This criterion was used in the design of the C-D nozzle for this simulation. To accommodate the specified diverging angles, the design began with total diverging angles of 10°, 14°, and 18°, while the throat size was determined based on the ratio between the nozzle inlet and the throat area. The selected throat sizes correspond to 20% (2 mm), 40% (4 mm), and 60% (6 mm) of the inlet diameter [31] (see Table 1).

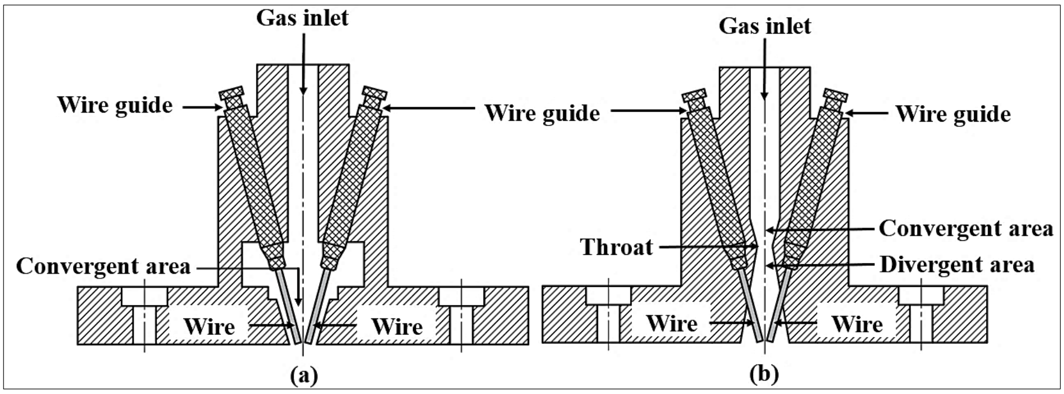

Figure 2. Schematic diagram of the nozzle in wire arc spraying: (a) TATF-400 nozzle and (b) convergent-divergent nozzle

Table 1. Dimensions of the convergent-divergent nozzle configuration model

Nozzle configuration	TATF-400	Convergent-Divergent
Gas inlet diameter	8 mm	8 mm
Convergent	30°	30°
Throat	-	2 mm, 4 mm, 6 mm
Divergent	-	10°, 14° and 18°
Throat into nozzle exit	-	40 mm
Arc angle	28°	28°

2.2. Modeling and Simulation Procedure

The three-dimensional (3D) modeling of a metal powder production machine using the wire arc spraying technique was performed using SolidWorks software and then imported into ANSYS FLUENT for Computational Fluid Dynamics (CFD) simulation [32]. The primary goal of mesh generation, for the study of metal powder production via wire arc spraying through a converging-diverging nozzle, is to capture the complex physics of particle-gas interactions and the flow behavior within the nozzle region and atomization chamber. The simulation domain is illustrated in Figure 3a. The meshing module in ANSYS FLUENT is divided into two sections. The first section, covering the nozzle area, employs the Hex Dominant meshing technique along with Edge Sizing processes in complex regions. Additionally, face meshing is utilized to ensure precise conformity to surface characteristics, enhancing the accuracy of the simulation results, especially in areas with rapid changes or critical importance. This method also effectively handles complex surfaces, allowing for efficient and accurate mesh generation in highly detailed geometries.

The second section, representing the atomization chamber, uses the Multizone meshing technique. This approach enables the generation of meshes with varying resolutions across different zones of the model, allowing mesh size adjustments as needed. The mesh's skewness was measured with an average value of 0.052, and the Orthogonal Quality achieved an average value of 0.994, indicating a high-quality mesh. Detailed local refinement is particularly necessary in regions with high turbulence and velocity gradients, especially when using the k-ω SST turbulence model. This refinement ensures accurate modeling of near-wall phenomena, with the mesh designed to keep particles within the refined regions throughout their flow path, ensuring precise particle tracking and preventing premature exit from the computational domain.

Figure 3b depicts the geometric structure and boundary conditions of the simulated spray chamber. Full-scale simulation of the spray chamber presents significant challenges due to the vast computational resources and time required, as the chamber has a diameter of up to 950 mm and a length of 5,500 mm. Thus, the simulation domain was reduced to a diameter of 300 mm and a length of 1,000 mm. These dimensions were deemed sufficient after preliminary evaluations to ensure that the reduction would not have a significant impact on the simulation results [16].

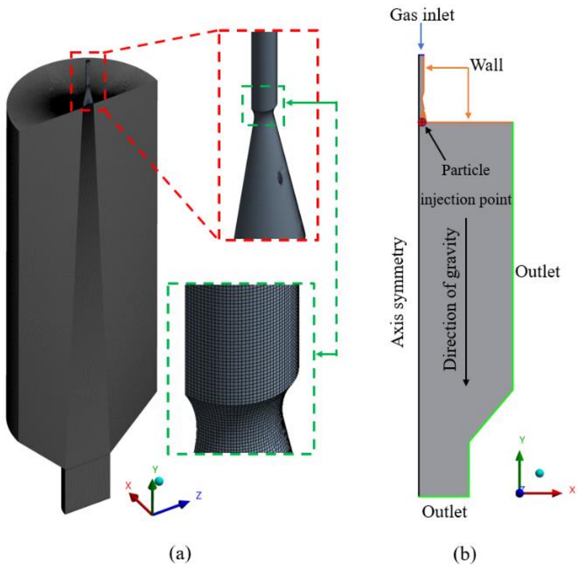

Figure 3. Wire arc spraying atomization model: (a) computational domain and (b) geometry structure with boundary conditions

2.3. Gride Independent

Figure 4 presents a mesh independence study conducted by examining the maximum velocity as a function of the number of elements for the TATF-400 nozzle. Such a study is essential in CFD simulations to ensure that the results are not significantly influenced by the mesh resolution, thereby achieving an optimal balance between computational cost and accuracy. The verification results indicate that the appropriate grid independence range for the simulation is reached when the number of elements is between approximately 1.1×10^7 and 1.2×10^7. At this point, the maximum velocity plateaus, signifying that the solution becomes independent of the mesh resolution, and further refinement does not lead to significant changes in the results. This study utilized a multi-zone meshing approach within the ANSYS FLUENT module to enhance resolution in specific regions of interest. This method is particularly advantageous for complex geometries, where precise mesh control was achieved using the Edge Sizing technique. The mesh size was set to 0.2 mm in the nozzle region and 1 mm at the domain boundary of the chamber, ensuring adequate resolution in critical areas while maintaining computational efficiency.

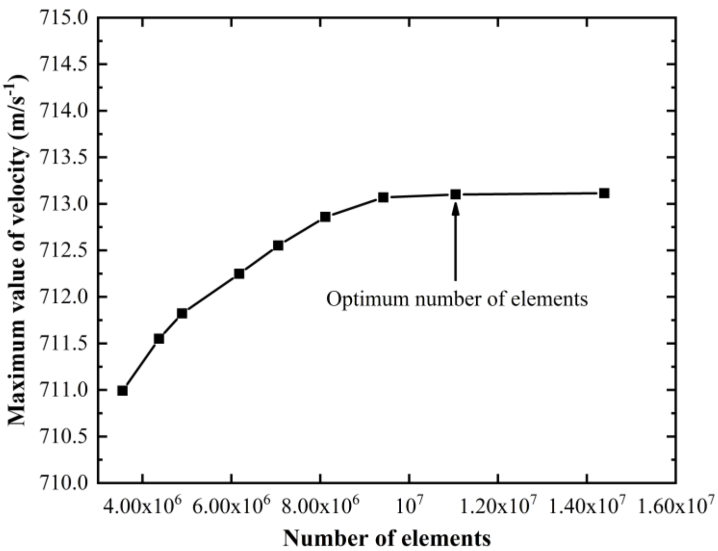

Figure 4. Grid independence verification

2.4. Solver and Boundary Condition Settings

The model was established relying on a complex configuration in ANSYS Fluent. The pressure-based solver operates in a transient mode, considering time-dependent variations and incorporating the gravitational effects along the Y-axis at a rate of -9.81 m/s, to precisely model the impact of gravity on particle motion. The k-ω SST model is utilized to precisely represent turbulent mixing and heat transfer phenomena, hence resolving turbulence. The Discrete Phase

Model approaches, such as stochastic tracking, coalescence, and breakup, are employed to simulate particle dynamics and predict their trajectories inside the flow field. The particle injection method follows the Rosin-Rammler distribution, with particles having an average temperature of 1,083°C. The injection flow rate is set at a constant value of 0.018 kg/s, and the particles have diameters that vary between 15 µm and 1 mm, with an average diameter of 0.5 mm. A spread parameter of 5.0 is utilized to ensure an accurate representation of particle distribution. The particle range, consisting of 10 diameter classes, is wide enough to accurately represent actual situations. Droplets undergo the Kelvin-Helmholtz and Rayleigh-Taylor (KH-RT) instabilities when they come into contact with steam, in order to imitate the fragmentation of particles under turbulent settings. This study employs the KH-RT model to predict the secondary breakup of droplets, while precisely representing the aerodynamic drag behavior using the spherical drag equation. The carrier fluid utilized is nitrogen gas (N_2), whereas the inert particle material employed is Ag925 (925 sterling silver).

The inlet boundary conditions specify a liquid pressure of 540,000 Pa before entering the nozzle system. The pressure is sufficient to breakup the particles into droplets. The particles have an initial velocity of 0.20 m/s, and the flow rate through the system remains constant. Numerical methods are employed to ensure accurate solutions for the pressure and velocity profiles in the convergent nozzle. The gradient computations utilize the least-squares cell-based method to accurately determine spatial variances. The PRESTO! algorithm is employed to address pressure differences in the mesh while handling occurrences that include substantial pressure variations. Simultaneously, a second-order upwind technique is utilized to precisely compute and sustain numerical stability and convergence for the resolved variables of density, momentum, turbulent kinetic energy, specific dissipation rate, and energy. The purpose of this simulation setup is to accurately represent the dynamic motion of particles and the characteristics of turbulence in the wire arc spraying process. By utilizing random particle tracking in the DPM framework, the simulation can accurately represent the random pathways of particles. The Rosin-Rammler distribution allows for a precise representation of the various particle sizes that are introduced into the system. Eventually, these modeling parameters will be employed in further simulations for C-D nozzles.

2.5. Model Assumption and Governing Equations

This study utilizes the DPM technique to simulate the manufacturing process of 925 sterling silver metal powder. Table 2 provides a detailed description of the physical characteristics of the powder. This study employed the WASA technique to examine the behavior of particles distributed in the gas flow field utilizing a C-D nozzle. The fundamental principle of DPM is to treat particles or clusters of particles as separate entities in the simulation, allowing for the tracking of their motion and other behaviors. To ensure the precision and uniformity of the simulation with respect to actual conditions, the following model assumptions might be established:

Table 2. Physical properties of silver sterling (Ag925)

Density (kg/m^3) at 20˚C	Thermal expansion (˚C^{-1})	Specific heat capacity (J/(Kg.k))	Electrical conductivity (%)	Tensile strength (MPa)	Elongation (%)	Hardness (HV)	Liquidus temperature (˚C)	Solidus temperature (˚C)
10.37×10^3	1.9×10^{-5}	245	96	283	40	71	788	891

- Nitrogen gas experiences expansion, and its velocity increases at the exit of the nozzle when flowing at supersonic velocity.
- Supersonic nitrogen gas is a compressible fluid that follows the ideal gas law due to its atomization characteristics.
- In the simulation of secondary atomization, it is assumed that the mass flow rate of the melt remains constant.
- The presence of shock waves in the gas flow resulting from supersonic velocity is believed to have no impact on the dispersion of particles.

The governing equations used to simulate the flow of the continuous phase, nitrogen (N_2), are the Navier-Stokes equation. This equation considers the conservation of mass, momentum, and energy. The k-ω SST (Shear Stress Transport) turbulence model is utilized, requiring the implementation of multiple sets of equations. Every arrangement allows for the accurate computation of the flow characteristics and heat transfer parameters of the fluid.

The resulting control equation is as follows:

Continuity equation :

$$\frac{\partial \rho}{\partial t} + \nabla(\rho \vec{v}) = 0 \tag{1}$$

Navier-Stokes equation:

$$\frac{\partial(\rho \vec{v})}{\partial t} + \nabla(\rho \vec{v}\vec{v}) = -\nabla p + \nabla(\mu_{eff}(\nabla \vec{v} + (\vec{v})^T) - \frac{2}{3}\delta_{ij}\mu_{eff}(\nabla \vec{v})) + \vec{F} \tag{2}$$

Energy equation:

$$\frac{\partial(\rho E)}{\partial t} + \nabla(\vec{v}(\rho E + p)) = \nabla\left[\mu_{eff}\left(\frac{\vec{v} + (\vec{v})^T}{2}\right) + k_{eff}\nabla T\right] + S_E \tag{3}$$

The k-ω SST (Shear Stress Transport) model is competent in precisely computing shear forces and energy dissipation in turbulent flow simulations. This feature enables it ideal for the analysis of nitrogen gas flow via a C-D nozzle and the dispersion of metal particles. This model is essential for accurately representing the complicated phenomena of turbulence and fluid dynamics. The C-D nozzle is a complex apparatus that enhances the gas flow rate to significant levels, leading to substantial variations in velocity across different regions of the flow. The Reynolds number (Re) typically exceeds 5000 in this operation, signifying the existence of turbulent flow conditions. This confirms the choice of the k-ω SST model. Precise simulations with a high level of accuracy are essential for comprehending the impact on the quality of the metal powder being generated.

Turbulent kinetic energy (k):

$$\frac{\partial(\rho k)}{\partial t} + \nabla(\rho k\vec{v}) = P_k - \beta \times \rho k\omega + \nabla((\mu + \sigma_k\mu_t)\nabla k) \tag{4}$$

Specific dissipation rate (ω):

$$\frac{\partial(\rho\omega)}{\partial t} + \nabla(\rho\omega\vec{v}) = \alpha\frac{\omega}{k}P_k - \beta\rho\omega^2 + \nabla((\mu + \sigma_\omega\mu_t)\nabla\omega) + (2(1 - F_1)\rho\sigma_\omega 2\frac{1}{\omega}\nabla k\nabla\omega \tag{5}$$

Turbulent viscosity:

$$\mu_t = \frac{\rho k}{\omega} \tag{6}$$

Effective thermal conductivity:

$$k_{eff} = k + \frac{\mu_t c_p}{Pr_t} \tag{7}$$

2.6. Discrete Phase Model (DPM)

The DPM is utilized to simulate the motion of particles in fluids using the Lagrangian method, wherein each particle is tracked along a trajectory in the continuous phase flow field. The particle tracking process in DPM is executed carefully to enhance the accuracy and uniformity of the simulations. The motion of particles in DPM is governed by equations that consider various forces, such as drag force, buoyancy force, and other external factors. The particle relaxation time (τ_r) in the fluid, as given by Equation 9, quantifies the duration required for a particle to adapt to changes in ambient conditions or variations in the velocity of the surrounding fluid. This value represents the magnitude of the aerodynamic drag force exerted on the particle. The drag coefficient, calculated using Equation 10, plays a crucial role in determining the drag force experienced by particles in the fluid. The value of C_d is governed by the Reynolds number (Re), as stated in Equation 11. This equation is utilized to analyze the rheological characteristics of particles in a fluid or the fluid dynamics surrounding the particles. The transfer of heat between the particles and the surrounding environment is a crucial aspect in the wire arc spraying process, which is used to produce metal powder. The variation in particle temperature (Tp) has an impact on this process. Equation 12 defines the diverse mechanisms via which heat is transferred, including convection and radiation.

$$m_p\frac{d\vec{v}_p}{dt} = m_p\frac{\vec{v} - \vec{v}_p}{\tau_r} + m_p\frac{\vec{g}(\rho_p - \rho_g)}{\rho_p} + \vec{F} \tag{8}$$

$$\tau_r = \frac{\rho_p {d_p}^2}{18\mu}\frac{24}{C_d Re} \tag{9}$$

$$C_d = a_1 + \frac{a_2}{Re} + \frac{a_3}{Re^2} \tag{10}$$

$$Re = \frac{\rho_g d_p|\vec{v}_p - \vec{v}|}{\mu} \tag{11}$$

$$m_p c_p\frac{dT_p}{dt} = hA_p(T_{local} - T_p) + \varepsilon_p A_p\sigma_p\left({\theta_r}^4 - {T_p}^4\right) \tag{12}$$

$$Nu = \frac{hd_p}{k_c} = 2.0 + 0.6Re^{1/2}Pr^{1/3} \tag{13}$$

$$Pr = \frac{c_c\mu}{k_c} \tag{14}$$

The computation of flow exiting a C-D nozzle is extremely complex since it involves the incorporation of both laminar and turbulent flows, as well as fluctuations in pressure and velocity in different sections of the nozzle. The Nusselt equation (Eq. 13) can be used to determine the heat transfer coefficient in particular areas of the nozzle, such as the throat or the diverging section. Using this framework, the calculated h value can be used to determine the heat transfer within the C-D nozzle. This is an essential element in designing the flow and heat transfer systems of the nozzle. Furthermore, to examine the flow characteristics and heat transfer within the nozzle, it is necessary to consider the Prandtl number (*Pr*), Reynolds number (*Re*), and Nusselt number (*Nu*) while analyzing the heat transfer in the fluid flow (Equation 14) during this procedure.

The KHRT breakup model for simulating droplet disintegration effectively incorporates the influence of the Kelvin-Helmholtz (KH) instability, which arises from aerodynamic forces, along with Rayleigh-Taylor (RT) instability. This is particularly due to the acceleration of droplets moving into a free environment. The breakup of droplets can be simulated by tracking the wavelength of the instability waves that grow most rapidly on the droplet surface. The KHRT model begins with the assumption that a Levich core exists near the transfer region, and it defines the core length (L), which allows for droplet disintegration as a result of the growth of Kelvin-Helmholtz waves. Wang et al. [33] is defined as follows:

$$L = C_L d_o \sqrt{\frac{\rho_1}{\rho_g}} \tag{15}$$

The breakup process is driven by the Kelvin-Helmholtz instability wave on the surface of the liquid core. The wavelength, λ_{KH} and the growth rate, ω_{KH} of the most rapidly growing Kelvin-Helmholtz wave are defined as follows:

$$We_q = \frac{\rho_q U^2 d_p}{\sigma p} \tag{16}$$

$$\lambda_{KH} = 9{,}02R \frac{(1+0{,}45Oh^{0,5})(1+0{,}47Ta^{0,7})}{(1+0{,}87We_g^{1,67})^{0,6}} \tag{17}$$

$$\omega_{KH} = \frac{(0{,}34+0{,}38We_g^{1,5})}{(1+Oh)(1+1{,}4Ta^{0,6})} (\frac{\sigma p}{\rho 1 R^3})^3 \tag{18}$$

$$Oh = \frac{We_1^{0,5}}{Re_1} \tag{19}$$

$$Ta = OhWe_g^{0,5} \tag{20}$$

$$r = B_{KH}\lambda_{KH} \tag{21}$$

where We represents the Weber number, the subscript q denotes one of the two phases, U is the relative velocity, R refers to the jet radius, Oh is the Ohnesorge number, Ta represents the Taylor number, r is the stable droplet radius, B_{KH} is the size constant, t_{KH} denotes the *KH* breakup time scale, and C_{KH} is the KH breakup time constant.

After the droplets are stripped from the liquid core and enter the free zone, RT instability becomes the main driving force of breakup. For the RT instability, the fastest growing wave ω_{RT} and the corresponding wave number K_{RT} are given by follows:

$$t_{KH} = \frac{3{,}726C_{KH}r}{\lambda_{KH}\omega_{KH}} \tag{22}$$

$$\omega_{RT} = \sqrt{\frac{2(-g_t(\rho_1-\rho_g))^{1,5}}{3\sqrt{3\sigma_p(\rho_1+\rho_g)}}} \tag{23}$$

$$K_{RT} = \sqrt{\frac{-gt(\rho_1-\rho_g)}{3\sigma_p}} \tag{24}$$

$$t_{RT} = \frac{C_t}{\omega_{RT}} \tag{25}$$

$$r_c = \frac{\pi C_{RT}}{K_{RT}} \tag{26}$$

2.7. Numerical Simulation Validation

Figure 5 presents the validation results of the TATF-400 nozzle model by comparing the calculated particle size distribution with experimental data from previous studies. The results indicate a high level of correlation between the simulation and experimental observations, particularly for the median particle size (D_{50}). The simulation closely matches the experimental data, with only minor deviations observed in the D_{50} values, confirming the robustness of the model in predicting the central trend of the particle size distribution. However, slight discrepancies were noted at the tails of the distribution (D_{10} and D_{90}), suggesting potential limitations of the model in accurately predicting the extreme ends of the particle size range, especially for very small or very large particles. Despite these minor inconsistencies, the overall particle size distribution pattern remains consistent with the experimental data, further validating the accuracy of the computational fluid dynamics (CFD) model. Summary of solver settings presented in Table 3.

Table 3. Summary of solver settings

Model	Settings
Discrete phase model	Stochastic collision; Coalescence; Breakup
Particle treatment	Unsteady particle tracking; Consider children in the same tracking step
Time	Transient, 2nd Order Implicit
Time step/s	5×10^{-7}
Drag law	Spherical
Secondary breakup model	KH-RT
Viscous model	k-ω SST
Pressure-Velocity coupling	Coupled
Pressure discretization	PRESTO!
Momentum discretization method	2nd Order Upwind
Outlet boundary type	Escape

Validation was conducted using data obtained from a laser particle size analyzer (model LA-350), with minimal deviations observed, thus ensuring confidence in the model's accuracy for real-world predictions. Therefore, this model will be applied in future simulations with the C-D nozzle to analyze the effects of nozzle geometry on the characteristics of the produced metal powder.

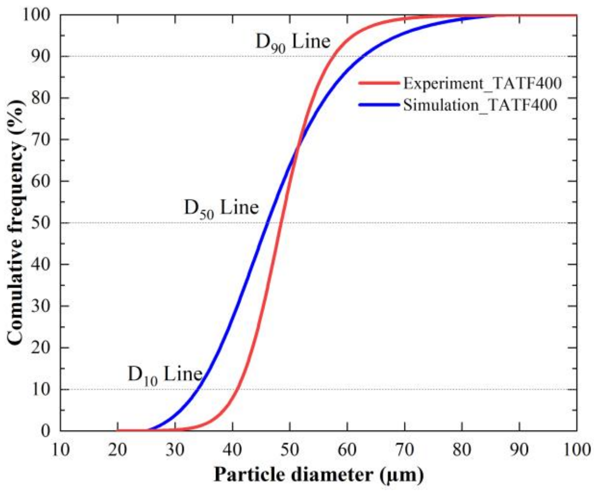

Figure 5. Validation of the particle size distribution for the TATF-400 nozzle

3. Results and Discussion

The integration of the C-D nozzle into the WASA process is an innovative and challenging technique for manufacturing metal powder, drawing considerable interest. This study examines the manufacturing of metal powder utilizing a C-D nozzle in the WASA process through CFD analysis. A key aspect of this study involves analyzing the nozzle's geometry while it is being used, as this has an important impact on the quality of the metal powder. The simulation findings are presented in a comprehensive manner as follows:

3.1. Gas Velocity Magnitude

Figure 6 illustrates the analytical findings of the gas (N_2) velocity field for the C-D nozzles designed in this study. The throat diameter of these nozzles is 2, 4, and 6 mm, and their divergent angles are 10°, 14° and 18°. The convergent angle remains constant at 30 degrees. They are specifically designed for flow conditions that maintain constant entropy, also known as isentropic flow. Initially, the fluid's velocity rises as it enters the nozzle's inlet, where the flow is subsonic ($M < 1$), and moves towards the convergent region where the cross-sectional area decreases. The fluid flows at an increased speed until it reaches the narrowest section of the nozzle, known as the throat. At this juncture, the velocity of the flow achieves the speed of sound ($M = 1$), indicating the critical condition. As the fluid flows through the throat and enters the wider section, the flow achieves a supersonic (M > 1), continuing to accelerate until it exits the nozzle. The velocity fields of each nozzle exhibit noticeable differences, indicating that the throat and divergence angle have an important impact on the gas velocity both inside and outside the nozzle. Furthermore, the presence of shock waves in the form of over-expansion is noticed as shown in Figure 7, which occurs as the gas accelerates through the narrowest part of the system and into the wider section. This results in a sudden acceleration in speed and a corresponding reduction in pressure. As the gas expands, it reaches a pressure at the nozzle exit that is higher than the pressure of the surrounding atmosphere. The pressure difference causes shock waves to form in the gas flow field. Based on the modeling findings shown in Figure 6 (a-c), the nozzle with a throat diameter of 2 mm reached a peak velocity of 995.35 m/s, while also exhibiting slight over-expansion shock waves.

Figure 6 (d-f) demonstrates that the gas velocity field of a C-D nozzle with a throat size of 4 mm that experiences a minor decrease when comparing to a nozzle with a 2 mm throat. The occurrence of shock waves in the form of over-expansion is more intense and prolonged, resulting in an increase in the length of the free jet boundary. Figure 6 (g-i) demonstrates that the flow field velocity is lower for a nozzle with a throat size of 6 mm compared to the 2 mm and 4 mm throat nozzles. Nevertheless, the shock wave intensity reaches its peak and the length of the free jet boundary is the highest. The gas velocity achieved is within the range of 792-799 m/s. In addition, all the nozzles simulated in this work are capable of utilizing the energy generated by gas expansion during atomization. In contrast to the study conducted by Schwenck et al. [34], which developed a unique convergent-divergent annular nozzle to minimize flow separation and recirculation using spraying pressures of 0.6 and 1.6 MPa and an inlet groove width ranging from 0.4 to 0.8 mm, they were only able to reach a maximum velocity magnitude of 700 m/s. In addition, there were issues with effectively utilizing the gas expansion energy in the atomization zone, specifically with the CCA-0.4 and CCA-0.8 nozzles.

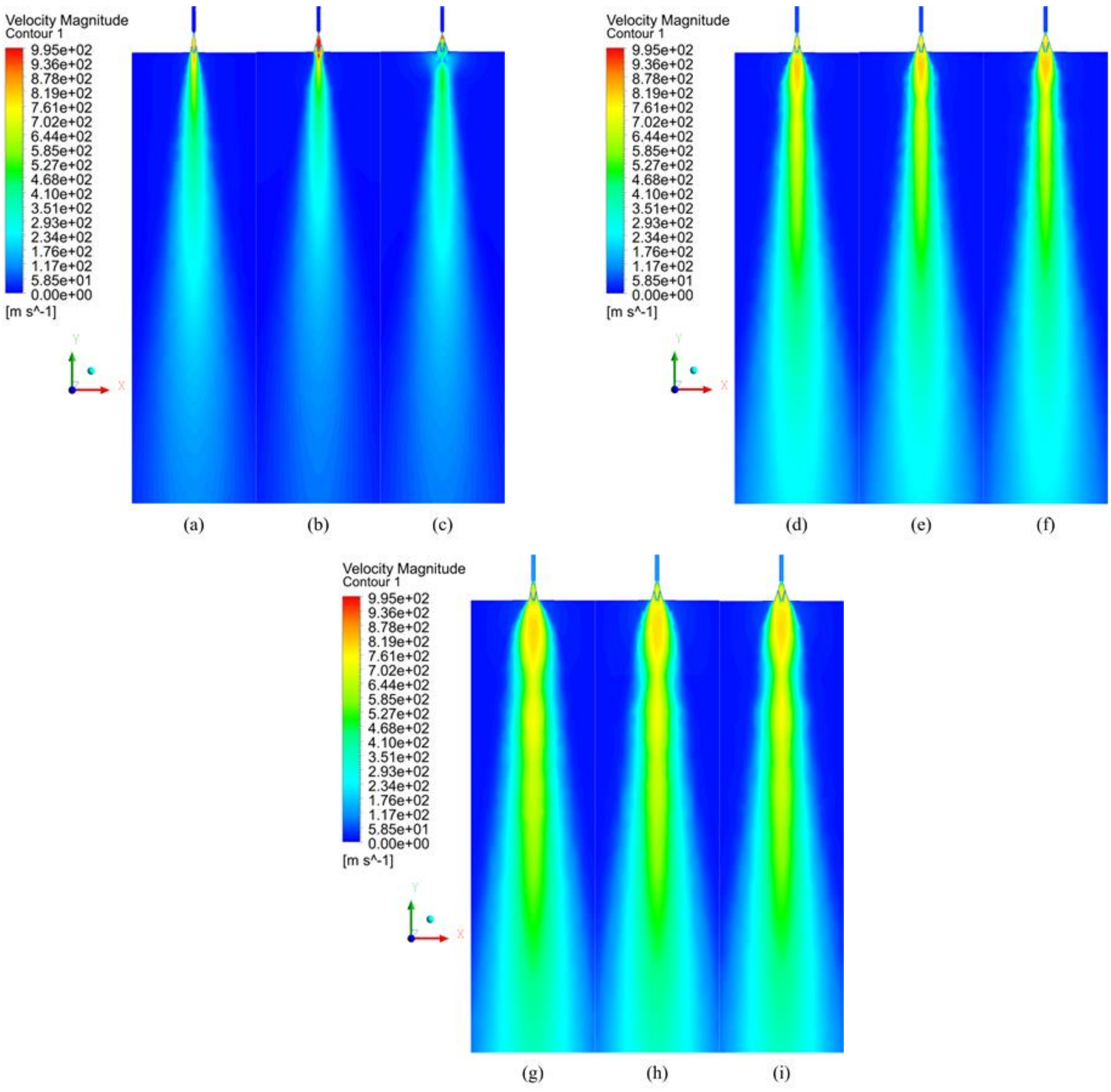

Figure 6. Gas velocity field in C-D nozzles: (a-c) throat 2 mm, (d-f) throat 4 mm, and (g-i) throat 6 mm, with divergent angles of 10°, 14°, and 18°

3.2. Shock Wave

Figure 7 illustrates the C-D nozzle used in this simulation of metal powder production, highlighting the occurrence of a shock wave indicative of over-expansion. The shock wave generated in this scenario is advantageous to the process as it causes a sudden change in the velocity of larger droplets relative to the gas. This increase in velocity can enhance the Weber number (We), which is crucial for droplet breakup. A higher Weber number indicates a greater likelihood of droplet fragmentation into finer particles, consistent with the findings of Kaiser et al. [35]. Additionally, the shock wave can induce instabilities in the liquid droplets, such as Rayleigh-Taylor (R-T) and Kelvin-Helmholtz (K-H) instabilities. These instabilities promote rapid deformation and fragmentation of the droplets, which is beneficial for processes requiring droplet atomization into smaller sizes. The results of this investigation align with the research of Wei et al. [36].

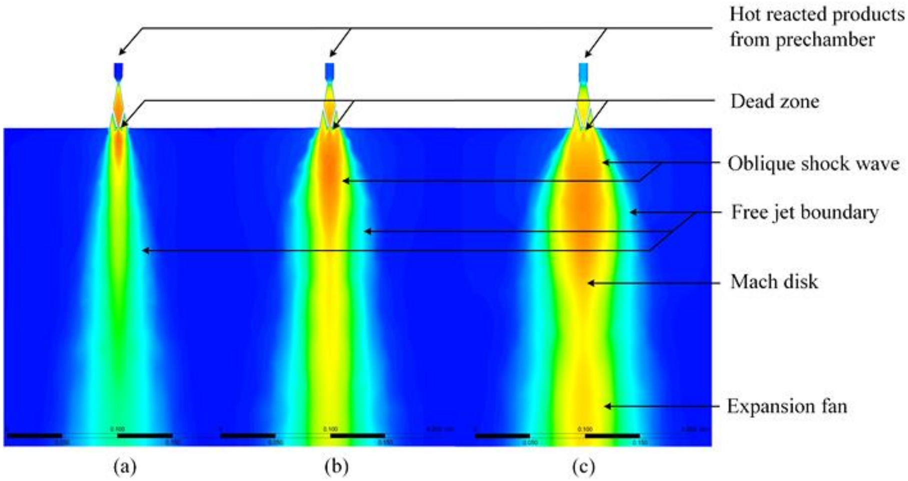

Figure 7. Over-expansion behavior with a constant divergent angle of 10°: (a) throat 2 mm, (b) throat 4 mm, and (c) throat 6 mm

Figure 8 demonstrates the characteristics of nitrogen gas flow patterns between all designed nozzles. The gas velocity experiences a dramatic increase as the fluid enters the throat. The nozzle with a throat diameter of 2 mm has the maximum velocity magnitude, followed by the nozzles with throat diameters of 4 and 6 mm, respectively. Nevertheless, it has been shown that the flow velocity experiences a significant reduction immediately after leaving the nozzle for the 2 mm throat nozzle. The sudden decrease in velocity is unfavorable to the WASA process, as this process necessitates a consistent high velocity over a specific distance to facilitate the appropriate formation of metal powder particles after being sprayed. In contrast, the nozzles equipped with throats of 4 and 6 mm are able to maintain the velocity of the flow over a greater distance.

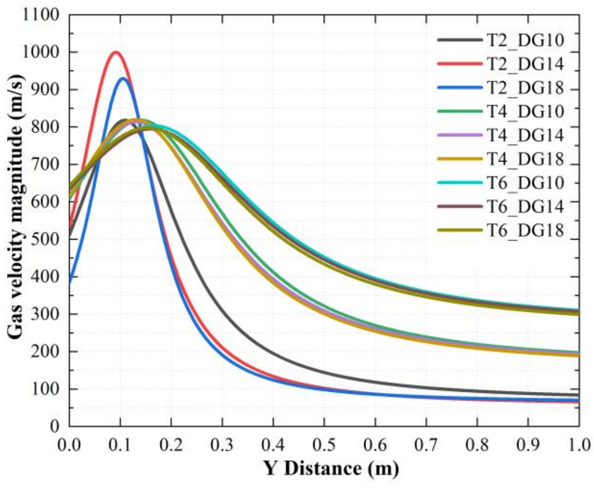

Figure 8. Flow field profile of all C-D nozzles conducted in this study

The gas flow field, once it leaves the nozzle, exhibits a progressive and uninterrupted reduction in gas velocity. This is a favorable attribute for the WASA process. Upon analyzing the gas velocity field after the nozzle exit, it is evident that the nozzle with a throat diameter of 6 mm maintains a greater velocity in comparison to nozzles of different throat diameters. At a distance of 1 meter from the nozzle outlet, the velocity can reach a maximum of 300 m/s and remain constant. The study conducted by Urionabarrenetxea et al. [16] examined the gas flow dynamics during atomization employing a close-coupled C-D nozzle. The investigation focused on inlet gas pressures ranging from 0.5 to 8 MPa. It was discovered that the highest speed achieved was 600 m/s while utilizing an inlet gas pressure of 8 MPa, and noticeable fluctuations in amplitude were observed. In contrast, the simulation conducted in this research employed an inlet gas pressure of 540,000 Pa (0.54 MPa) and achieved velocity magnitudes ranging from 792 to 995 m/s, which is a favorable outcome when compared to the previously described study.

3.3. Total Pressure

Figure 9 illustrates the total pressure, which indicates the overall energy of the fluid in the C-D nozzle system. It can be noted that the highest pressure point is located about at Y = 0.06 m (or 60 mm) from the nozzle inlet. The pressure at the throat rises quickly as the flow is compressed through the narrowest part, resulting in an increase in velocity. The maximum pressure at this point ranges from 7.5 to 8.9 MPa. Once the fluid moves through the narrow throat and enters the wider diverging section, its speed slows as the area it occupies expands, resulting in a corresponding decrease in pressure. This behavior conforms to the theory of energy conservation and the transformation of kinetic energy into potential energy (static pressure) until the fluid reaches the location of 0.1 m (or 100 mm), which is the nozzle exit. Additionally, it is observed that a smaller divergence angle of 10° leads to increased pressure since the fluid expands more rapidly compared to greater divergence angles of 14° and 18°. The pressure at the throat of a nozzle with a 4 mm size ranges from 1.5 to 2 MPa, while for a nozzle with a 6 mm size, the pressure ranges from 1 to 1.5 MPa. A key finding in this study is the notable influence of throat size on total pressure as the throat size expands, the total pressure diminishes. Nevertheless, the increase in the divergent angle has only a slight effect on the total pressure. The total pressures obtained were greater than those reported by Zangana et al. [7]. Their study focused on the effect of convergent-divergent tubes on the cooling efficiency of vortex tubes. They achieved this by decreasing the throat size from 8 mm to 2.5 mm and utilizing an inlet pressure of 0.6 MPa. According to their research, the overall pressure varied within the range of around 70 kPa (70,000 Pa), potentially as a result of variations in the design of the nozzle. The geometry of the C-D nozzle has a substantial impact on the pressure both inside and outside the nozzle.

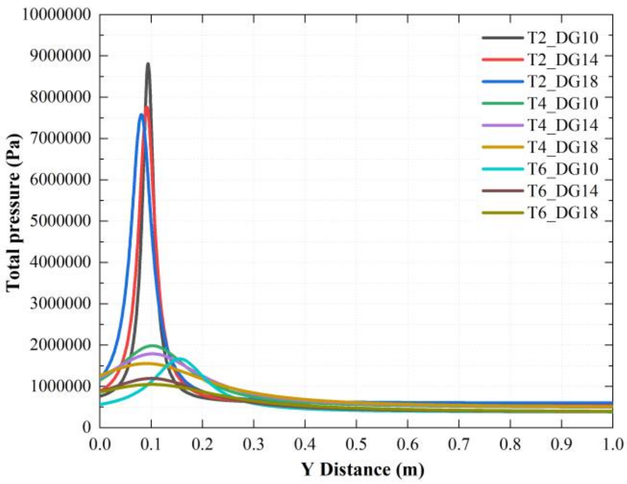

Figure 9. Total pressure profile of all C-D nozzles conducted in this study

3.4. Effect of Nozzle Shape on Particle Diameter and Particle Distribution

This study examines the geometric configuration of C-D nozzles and its influence on the size of metal powder particles generated using the WASA process, employing CFD analysis. The desired median particle size (D_{50}) for the metal powder is 45 µm, which is often employed in additive manufacturing (AM) techniques including Selective Laser Melting (SLM) and Wire Beam Melting (WBM) [37-40]. Based on the data shown in Table 4 and Figure 10, it is clear that a rise in the divergent angle of the nozzle leads to a reduction in the size of metal powder particles. This phenomenon occurs as a result of the increased expansion area for the fluid, resulting in elevated velocities and the sustained velocity over longer distances. This extended duration provides more time for the formation of particles, as previously described. Increased velocities intensify the shear stress exerted on the molten metal, hence improving the atomization process and resulting in the formation of smaller droplets. The simulation findings clearly demonstrate that the nozzle's geometry has a substantial impact on both the size and distribution pattern of the metal powder particles. The nozzle with a bigger size (T6_DG14) achieved the desired particle size most accurately, with a D_{10} value of 21.25 µm, a D_{50} value of 44.42 µm, and a D_{90} value of 93.21 µm. Under the simulated conditions, this nozzle exhibited the narrowest particle size distribution.

Table. 4 Computational results of particle size distribution for different throat and divergent configurations

Nozzle size	Average Mass flow rate (kg/s)	D_{10} (µm)	D_{50} (µm)	D_{90} (µm)	Cooling Rate (°C/s)
T2_DG10	0.003	29.27	55.09	119.86	88.6
T2_DG14	0.003	25.02	75.07	176.67	87.5
T2_DG18	0.003	28.77	88.83	188.93	84.6
T4_DG10	0.015	20.77	43.06	96.07	87.2
T4_DG14	0.015	25.27	54.94	98.58	84.7
T4_DG18	0.015	27.52	55.09	107.91	81.0
T6_DG10	0.029	20.27	40.85	103.80	81.6
T6_DG14	0.029	21.52	44.42	93.21	70.3
T6_DG18	0.029	21.02	44.29	116.98	77.1

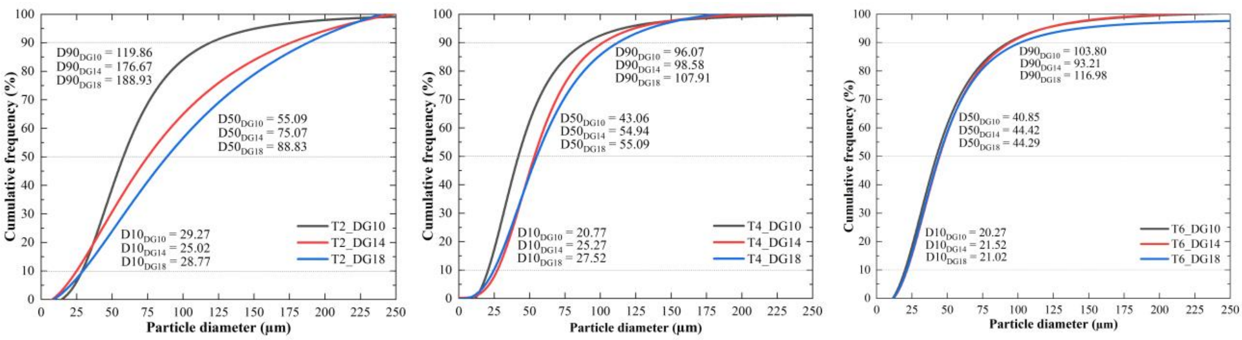

(a) (b) (c)

Figure 10. Particle size distribution: (a) throat 2 mm, (b) throat 4 mm, (c) throat 6 mm

The simulation of metal powder production using the wire arc spraying technique in this study yielded metal powder with a D_{50} particle size range of 40-88 µm, depending on the nozzle shapes employed. In contrast, the optimal particle size for use in additive manufacturing processes varies for selective lase-r melting (SLM), the suitable range is 20-45 µm; for electron beam melting (EBM), it is 45-100 µm [37, 41, 42] and for laser powder bed fusion (LPBF), it is 40-50 µm [40, 43]. These ranges align with the specific limitations of AM processes, where the layer thickness typically does not exceed 100 µm. Nevertheless, the particle size obtained from the wire arc spraying process can still be used for AM. Furthermore, studies by Fan et al. [44] and Iebba et al. [45] demonstrate that varying particle size distributions help fill gaps between larger particles, improving powder flow efficiency in the forming bed and increasing powder layer density during forming. This results in the fabrication of components with higher and more uniform density. Parts produced from powders with varying particle sizes tend to exhibit superior mechanical properties, such as enhanced strength and durability. These findings have been corroborated by Sofia et al. [46].

The C-D nozzle offers significant advantages over the Close-Coupled Gas Atomization (CCGA) nozzle in controlling fluid flow. The C-D nozzle can reduce gas flow uncertainties, providing a more stable and consistent flow profile, which is crucial for achieving uniform dispersion of molten metal. This results in more consistent and predictable particle sizes. A narrow particle size distribution enhances production quality. In contrast, a study by Samuel J. et al. [20], which simulated the CCGA process using a CFD model based on the Euler-Lagrange approach, found that the CCGA nozzle experienced multiple turbulence interactions between the gas and molten metal. These interactions led to instability in both gas and metal flow. Such fluctuations adversely affect the atomization efficiency of the molten metal and may result in an uneven particle size distribution. Figures 11 to 13 show the analysis of particle breakup and distribution using the Weber number (We), which is a dimensionless quantity that compares the significance of inertial forces to surface tension forces in the fluid. When the diverging angle of small throat nozzles grows from 10° to 18°, the Weber number experiences a considerable increase, suggesting that inertial forces become stronger than surface tension forces. As a consequence, there is an amplification in particle breakup, while bigger droplets have a tendency to aggregate in close proximity to the central region of the nozzle. On the other hand, bigger nozzles display a more extensive distribution of particles, resulting in smaller droplets that distribute widely from the nozzle's center. The Weber number for these larger throat nozzles exceeds that of the small and medium throat nozzles, indicating that inertial forces more efficiently counteract the surface tension of the droplets.

Currently, there are ongoing investigations into secondary atomization processes in the manufacturing of amorphous powders that comprise mainly up of Fe. The primary objective is to comprehend the movement of particles and the mechanisms involved in their cooling. Pu Wang et al. [33] showed that the average size of particles reduces with an increase in the gas-to-metal ratio (GMR). In addition, increasing the pressure used to atomize the metal and decreasing the rate at which the molten metal flows leads to the production of smaller particles. Most of these particles have a D_{50} size greater than 50 µm. On the other hand, the process of producing metal powder through WASA process using a C-D nozzle has many benefits compared to the study conducted by Pu Wang et al. These advantages include the creation of smaller powder particles (D_{50} = 44.42 µm), the utilization of lower pressure (0.54 MPa), and the use of lower mass flow rates (0.029 kg/s). Shuai Zhang et al. [47] conducted a simulation to produce 316L stainless steel powder particles. They used a close-coupled atomizer to examine the impact of high-pressure gas on metal powder synthesis. The investigation involved pressures ranging from 3 to 6 MPa and nozzle sizes of 4 and 4.6 mm. Through their calculations, it was discovered that increasing the pressure leads to a more refined distribution of particle sizes. At a pressure of 3 MPa, the D_{50} particle size was 77 µm, which was greater and necessitated a higher pressure compared to the metal powder generation utilizing the C-D nozzle in this study.

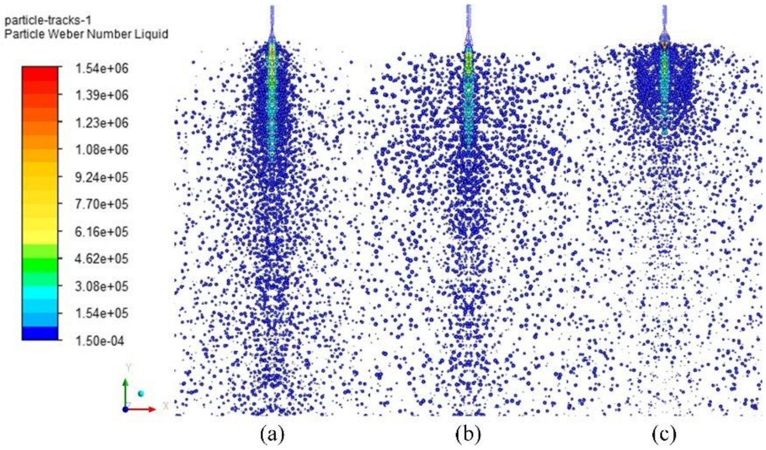

Figure 11. Particle fragmentation in liquid as a function of Weber number for throat 2 mm, with divergent angles of (a) 10°, (b) 14°, and (c) 18°

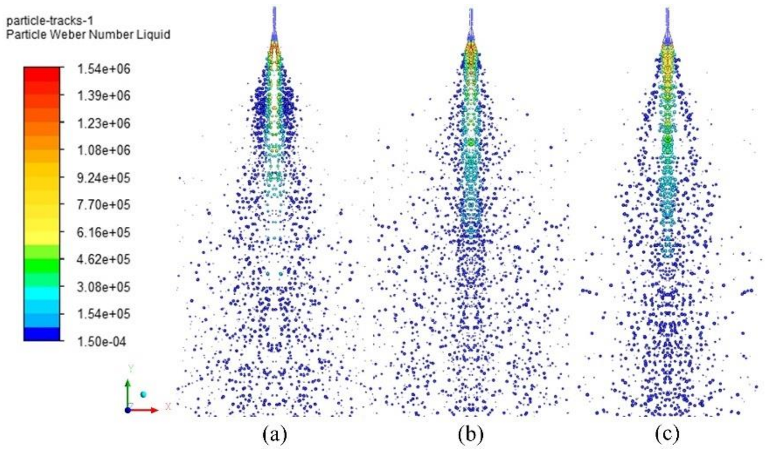

Figure 12. Particle fragmentation in liquid as a function of Weber number for throat 4 mm, with divergent angles of (a) 10°, (b) 14°, and (c) 18°

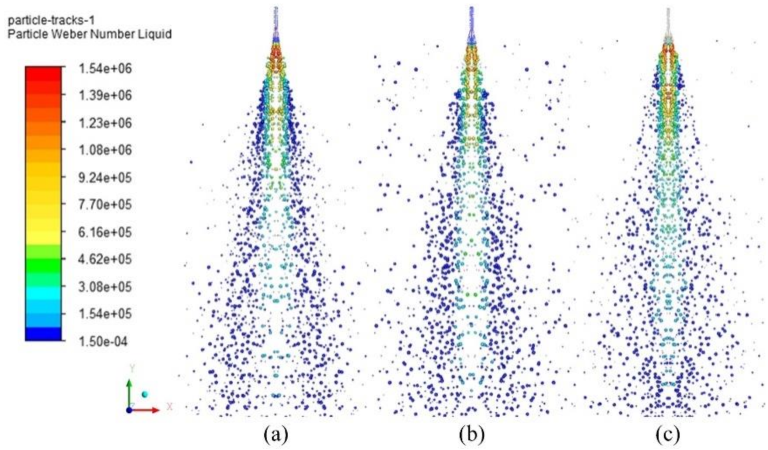

Figure 13. Particle fragmentation in liquid as a function of Weber number for throat 6 mm, with divergent angles of (a) 10°, (b) 14°, and (c) 18°

The transition from a high-velocity jet at the nozzle throat to a lower velocity upon entering the surrounding environment results in a reduction in the shear forces acting on the fluid, leading to the formation of larger droplets. As the shear force decreases, the energy required to break the liquid into droplets also diminishes, contributing to the generation of larger droplets or particles. Moreover, the reduction in shear forces leads to a broader particle size distribution, consistent with the findings of Daskiran et al. [48] and Hanthanan et al. [49], as well as the experimental results shown in Figure 10. Gonabadi et al. [50], Mehrabi et al. [51], and Iebba et al. [45] have demonstrated that parts produced with larger particles tend to have a rougher surface finish, which may negatively affect both aesthetic quality and functional performance. Additionally, larger particles exhibit reduced flowability, leading to inconsistent feed rates into the printer and problems such as uneven layer thickness and defects in the printed structure. Furthermore, Rando et al. [52] confirmed that particle size also influences heat transfer during the printing process, causing warping and internal stresses as particles cool and solidify at different rates.

3.5. Effect of Nozzle Shape on Particle Temperature

Figure 14 illustrates the temperature distribution of metal particles throughout the atomization process. The charts show various cooling temperatures that arise from the different characteristics of the nozzle geometries. The initial high temperature, around 1200°C, signifies the total temperature of the molten metal prior to the beginning of atomization. Nozzles with smaller throat diameters (T2) demonstrate a higher rate of particle cooling in comparison to nozzles with medium (T4) and large (T6) throat diameters. Rapid particle cooling induces rapid solidification of the particle surface, limiting the formation of particles in the desired manner, hence leading to the production of bigger particle sizes. During the initial stage (0-0.1 milliseconds), there is a notable rise in heat transfer efficiency, which corresponds to the analysis of the particle Nusselt Number illustrated in Figures 15 to 17. As a result, the temperature dramatically drops to less than 400°C within 0.25 milliseconds. In contrast, nozzles that are large and have greater cross-sectional surfaces undergo significant over-expansion of the gas and exhibit slower rates of heat transfer Furthermore, the Weber number reaches a value of 1.54×10^6. These behaviors are beneficial for the WASA process, as they provide sufficient time for the generation and fragmentation of particles. The particle size and distribution are influenced by these parameters, as evidenced by Figure 10. In this figure, the overall D_{50} particle size in the largest throat nozzle is smaller and the distribution is narrower compared to small and medium throat nozzles. This suggests that the design of the nozzle is extremely important in regulating the thermal properties and particle velocity, which subsequently impacts the particle diameter.

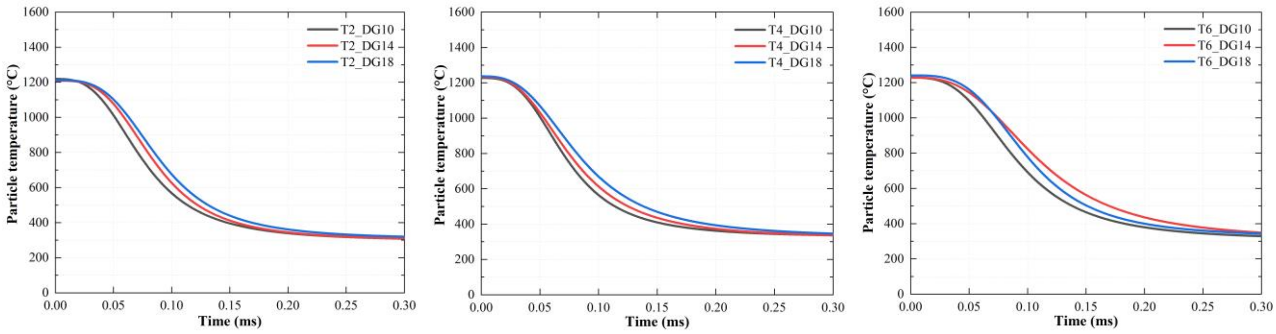

(a) (b) (c)

Figure 14. Particle temperature: (a) throat 2 mm, (b) throat 4 mm, (c) throat 6 mm

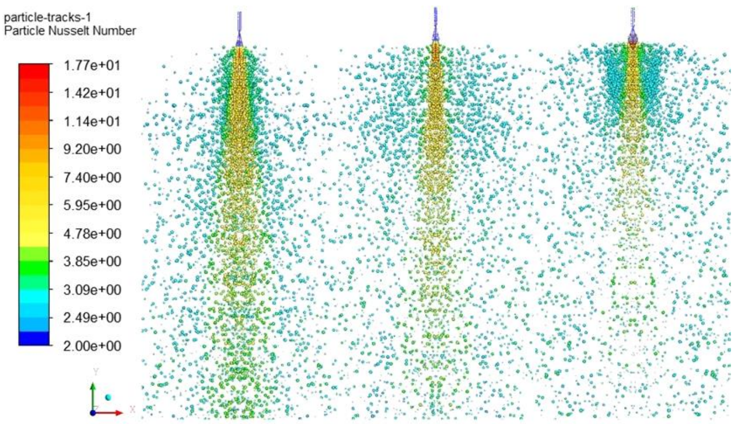

(a) (b) (c)

Figure 15. Heat transfer rate for throat 2 mm, with divergent angles of (a) 10°, (b) 14°, and (c) 18°

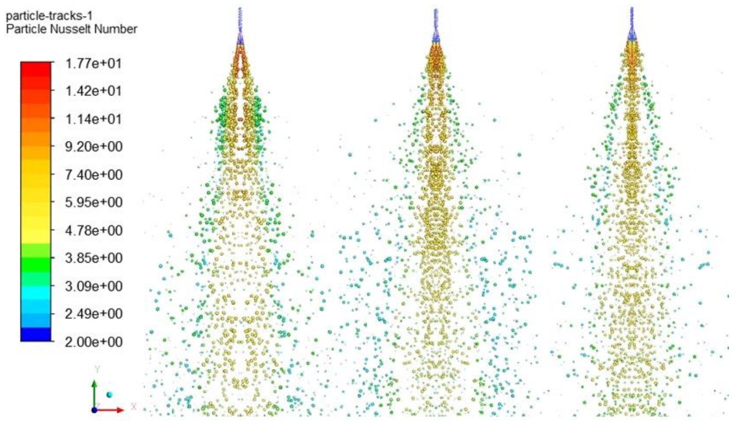

(a) (b) (c)

Figure 16. Heat transfer rate for throat 4 mm, with divergent angles of (a) 10°, (b) 14°, and (c) 18°

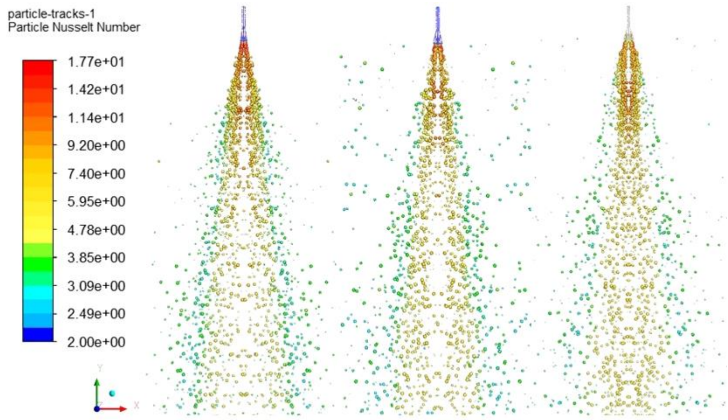

(a) (b) (c)

Figure 17. Heat transfer rate for throat 6 mm, with divergent angles of (a) 10°, (b) 14°, and (c) 18°

3.6. Effect of Nozzle Shape on Particle Velocity Magnitude

According to Figure 18, it can be shown that largest throat nozzles have a tendency to produce higher particle velocities in comparison to smaller and medium throat nozzles. The chart illustrates the relationship between particle velocity and nozzle size. It shows that larger nozzles result in higher particle velocities, especially during the time period of 0.05-0.10 ms, with an average peak velocity of approximately 60 m/s. Medium throat nozzles produce particle velocities of about 52 m/s, which is considered moderate. On the other hand, small throat nozzles have the lowest average particle velocities, measuring around 30 m/s. The relationship between these two factors is interconnected and has a direct influence on the size of the metal powder particles. Increased particle velocities are essential for particles to acquire sufficient kinetic energy to undergo uniform fragmentation and produce small particles during the atomization process.

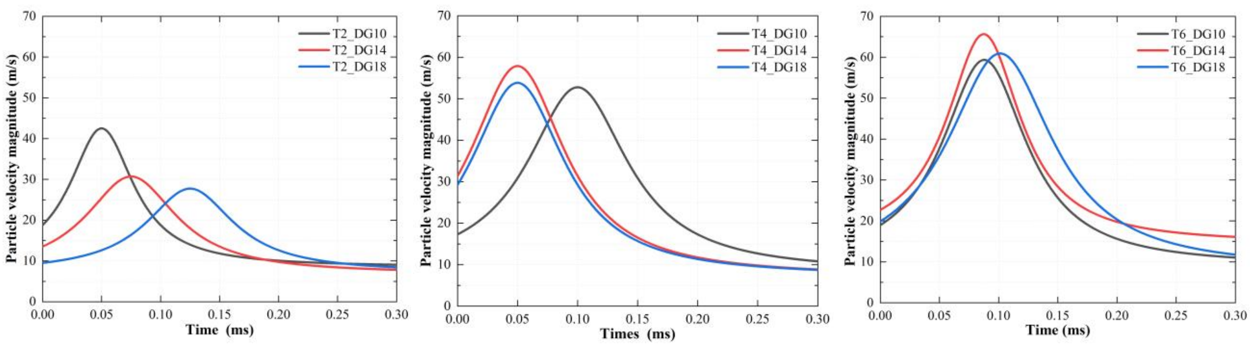

(a) (b) (c)

Figure 18. Particle velocity magnitude: (a) throat 2 mm, (b) throat 4 mm, (c) throat 6 mm

In addition, the movement of particles at low velocities leads to the formation of larger and more irregularly shaped particles. For large throat nozzles, the particle velocity is high because the particles are accelerated through the throat and the gas expands in the diverging section. However, the cooling rate is poor in these cases due to the high particle velocities at the nozzle exit. When gas flows at high speeds through large throat nozzles, the strong shear forces cause the liquid to fragment into smaller particles. Despite the small size of the particles, their elevated velocity decreases the amount of time they spend in a heat exchange environment, leading to less effective heat transfer. High-velocity particles rapidly move between points, hence decreasing the available time for transferring heat with the surroundings.

4. Conclusions

This study investigates the geometry of convergent-divergent nozzles in the metal powder production process employing wire arc spraying atomization through computational fluid dynamics. The study examines the impact of throat size and diverging size on the dimension and distribution of particles in 925 sterling silver metal powder. The findings can be summarized as follows:

- The validated TATF-400 nozzle model demonstrates a clear consistency between the simulated particle size distribution and experimental results, particularly with regard to the median particle size (D_{50}), which confirms the reliability of the computational fluid dynamics model. Additionally, validation using a laser particle size analyzer (LA-350) further supports the accuracy of the model, ensuring its predictive capabilities for real-world applications. Consequently, the validated TATF-400 nozzle model can be effectively applied to C-D nozzle modeling to investigate the impact of nozzle geometry on the characteristics of metal powders.

- The computational findings of C-D nozzles indicate that the dimensions of the throat and the angle of the divergent section have an important impact on the gas acceleration and the preservation of velocity upon departing the nozzle. Nozzles with a largest throat size (T6) have a superior ability to maintain gas velocity and expansion compared to medium (T4) and small (T2) throat nozzles. Moreover, larger throat nozzles encounter stronger shock waves in the shape of over-expansion. Small diverging angles (DG10) result in increased total pressure within the nozzle.

- The dimensions and distribution of particles clearly illustrate the influence of nozzle size and shape on the atomization process. Small throat nozzle and lower divergence angles lead to elevated velocities and enhanced shear forces inside the nozzle, which promptly diminish once the fluid exits the nozzle. On the other hand, larger throat nozzles have the ability to maintain greater speeds and shear forces even after the liquid leaves the nozzle. This results in metal powder particles that are closer to the desired size range for additive manufacturing (AM) processes, with D_{50} values ranging from 40 to 44 µm. Small throat nozzles provide D_{50} values ranging from 55 to 88 µm, whereas medium throat nozzles create D_{50} values ranging from 43 to 55 µm

- The configuration of the C-D nozzle has an important impact on the particle temperatures, specifically the size of the throat and the angle of divergence, as well as their influence on the cooling behavior of the particles. Small or medium throat nozzles have the ability to rapidly distribute or release heat, resulting in particle temperatures reaching around 360°C in just 0.25 milliseconds. Nevertheless, increasing the divergent angle to 14° and 18° slightly diminishes the cooling efficiency. Nozzles of larger throat size demonstrate a reduced rate of cooling, however they continue to maintain a relatively effective cooling processes. The rate at which particles cool is a critical factor that affects the size of particles in the manufacturing of metal powder. C-D nozzles have the ability to effectively control and adjust the cooling rates of metal powder particles.

- Particle velocity is a significant determinant of the size and distribution of metal powder particles. Particles discharged from small throat nozzles with narrow divergent angles (DG10) exhibit the greatest acceleration as compared to medium (DG14) and large (DG18) divergent angles. Nevertheless, these small throat nozzles produce particle velocities that are lower in comparison to nozzle sizes of bigger throat sizes. Utilizing larger throat nozzles enhances stability and equilibrium in achieving particle velocity. Increasing the throat size also enhances the distribution of pressure and inertial forces within the fluid, resulting in a reduction in flow resistance and enabling the fluid to flow through the nozzle at a higher speed, thus increasing particle velocity.

5. Nomenclatures

ρ	Density	h	Convective heat transfer coefficient
t	Time	A_p	Surface area of the particle
$\vec{v}$	Velocity vecto	T_{local}	Local temperature of the fluid
p	Fluid pressure	T_p	Temperature of the particle
∇p	Pressure gradient force	ε_p	Emissivity
$\nabla\vec{v}$	Velocity gradient tensor	A_p	Surface area of the particle
μ_{eff}	Effective dynamic viscosity	Nu	Nusselt number
δ_{ij}	Kronecker delta	h	Convective heat transfer coefficient
$\vec{F}$	External body forces	d_p	Diameter of the particle

E	Total energy	k_c	Thermal conductivity of the fluid
k_{eff}	Effective thermal conductivity	Pr	Prandtl number
∇T	Temperature gradient	L	Characteristic length scale
S_E	Energy source term	d_o	Diameter of the nozzle or orifice
k	Turbulent kinetic energy	We	Weber number
P_k	Production term	ρ_q	Density of the fluid
$\beta *$	Model constant	σp	Surface tension
ω	Specific dissipation rate	λ_{KH}	KH wavelength
σ_k	Turbulence model constant	R	Jet or droplet radius
μ_t	Turbulent viscosity	Oh	Ohnesorge number
$\nabla\omega$	Gradient of the specific dissipation rate	ω_{KH}	Kelvin-Helmholtz instability growth rate
c_p	Specific heat capacity at constant pressure	r	Droplet radius
Pr_t	Turbulent Prandtl number	B_{KH}	Stable radius of droplets
m_p	Mass of the particle	t_{KH}	Breakup time
$\vec{v}_p$	Particle velocity	C_{KH}	KH instability constant
τ_r	Particle relaxation time	K_{RT}	Wave number
$\vec{g}$	Gravitational acceleration	ω_{RT}	Growth rate
ρ_p	Density of the particle	gt	Droplet acceleration
ρ_g	Density of the fluid (gas)	t_{RT}	RT breakup time scale
d_p	Diameter of the particle	C_t	Rt breakup time constant
C_d	Drag coefficient of the particle	r_c	Radius of child droplet
Re	Reynolds number	C_{RT}	Breakup radius constant

6. Declarations

6.1. Author Contributions

Conceptualization, M.S. and P.K.; methodology, P.K.; software, M.S.; validation, M.S. and P.K.; formal analysis, P.K.; investigation, M.S.; resources, M.S.; data curation, M.S.; writing—original draft preparation, M.S. and P.K.; writing—review and editing, M.S. and P.K.; visualization, M.S. and P.K.; supervision, M.S.; project administration, M.S.; funding acquisition, M.S. and P.K. All authors have read and agreed to the published version of the manuscript.

6.2. Data Availability Statement

The data presented in this study are available in the article.

6.3. Funding and Acknowledgements

This research was conducted under the support of the National Science and Technology Development Agency (NSTDA) of the Royal Thai Government for the scholarship of academic year 2021, the Department of Industrial Engineering, Faculty of Engineering, Rajamangala University of Technology Thanyaburi for supporting this research article and the National Research Council of Thailand (NRCT) for providing experimental instruments through the research project “Design, fabricate and manufacture of titanium/platinum powder particles for forming parts in target industries by additive manufacturing process” (Grant no. N23A64003).

6.4. Institutional Review Board Statement

Not applicable.

6.5. Informed Consent Statement

Not applicable.

6.6. Declaration of Competing Interest

The authors declare that they have no known competing financial interests or personal relationships that could have appeared to influence the work reported in this paper.

7. References

[1] Sasnauskas, A., Coban, A., Zhang, W., Abbot, W. M., Babu, R. P., Pham, M. S., & Lupoi, R. (2024). Metal additive manufacturing using powder sheets (MAPS) of HEA CoNiCrFeMn: The effect of the polymer content on microstructure and mechanical properties. CIRP Annals, 73(1), 173–176. doi:10.1016/j.cirp.2024.04.066.

[2] Zhang, W., Sasnauskas, A., Coban, A., Marola, S., Casati, R., Yin, S., Babu, R. P., & Lupoi, R. (2024). Powder sheets additive manufacturing: Principles and capabilities for multi-material printing. Additive Manufacturing Letters, 8, 100187. doi:10.1016/j.addlet.2023.100187.

[3] Deng, G., Dong, B., Zhang, C., Wang, R., Yang, Z., Nie, N., Wang, P., Wang, L., Wang, H., Tian, Y., Su, L., & Li, H. (2024). Microstructure, microhardness and high-temperature tribological properties of CoCrFeNiMnTi0.3 high entropy alloy coating manufactured by powder-bed arc additive manufacturing. Surface and Coatings Technology, 485, 130918. doi:10.1016/j.surfcoat.2024.130918.

[4] Yang, S. S., Lai, H. L., Chen, C. C., Lu, S. T., Dai, Y. M., Cheng, W. C., Fuh, Y. K., & Li, T. T. (2024). Wire-arc spray directed energy deposition: Correlation of chamber kits refurbishing and particle defects reduction in Ta/TaN thin-film physical deposition processes. Journal of Materials Research and Technology, 30, 2754–2767. doi:10.1016/j.jmrt.2024.03.180.

[5] Afshari, A. A., McKinney, W., Cumpston, J. L., Leonard, H. D., Cumpston, J. B., Meighan, T. G., Jackson, M., Friend, S., Kodali, V., Lee, E. G., & Antonini, J. M. (2022). Development of a thermal spray coating aerosol generator and inhalation exposure system. Toxicology Reports, 9, 126–135. doi:10.1016/j.toxrep.2022.01.004.

[6] Zhixiang, Z., Jiao, Z., Zhengwei, L., Yuandong, M., Guiming, L., Liangliang, W., & Zhongning, G. (2023). Study on the corrosion electrochemistry behavior and wear resistance of the arc thermal sprayed Zn–Al alloy coating. Journal of Materials Research and Technology, 24, 8414–8428. doi:10.1016/j.jmrt.2023.05.109.

[7] Zangana, L. M. K., & Barwari, R. R. I. (2020). The effect of convergent-divergent tube on the cooling capacity of vortex tube: An experimental and numerical study. Alexandria Engineering Journal, 59(1), 239–246. doi:10.1016/j.aej.2019.12.036.

[8] Tsuge, N. (2015). Existence of global solutions for isentropic gas flow in a divergent nozzle with friction. Journal of Mathematical Analysis and Applications, 426(2), 971–977. doi:10.1016/j.jmaa.2015.01.031.

[9] Biju Kuttan, P., & Sajesh, M. (2013). Optimization of divergent angle of a rocket engine nozzle using Computational Fluid Dynamics. The International Journal of Engineering and Science, 2(1), 196–207.

[10] Balabel, A., Hegab, A. M., Nasr, M., & El-Behery, S. M. (2011). Assessment of turbulence modeling for gas flow in two-dimensional convergent-divergent rocket nozzle. Applied Mathematical Modelling, 35(7), 3408–3422. doi:10.1016/j.apm.2011.01.013.

[11] Sazonov, Y. A., Mokhov, M. A., Bondarenko, A. V., Voronova, V. V., Tumanyan, K. A., & Konyushkov, E. I. (2023). Interdisciplinary Studies of Jet Systems using Euler Methodology and Computational Fluid Dynamics Technologies. HighTech and Innovation Journal, 4(4), 703–719. doi:10.28991/HIJ-2023-04-04-01.

[12] Chen, Y., Liang, X., Liu, Y., & Xu, B. (2009). Numerical analysis of the effect of arc spray gun configuration parameters on the external gas flow. Journal of Materials Processing Technology, 209(18–19), 5924–5931. doi:10.1016/j.jmatprotec.2009.07.009.

[13] Malik, N. M., Zaheer, M. A., & Farooq, M. A. (2024). Effect of Convergent Angle on different Flow Parameters of a Convergent-Divergent Nozzle. MATEC Web of Conferences, 398, 01001. doi:10.1051/matecconf/202439801001.

[14] Khalid, M. W., & Ahsan, M. (2020). Computational Fluid Dynamics Analysis of Compressible Flow Through a Converging-Diverging Nozzle using the k-ε Turbulence Model. Engineering, Technology and Applied Science Research, 10(1), 5180–5185. doi:10.48084/etasr.3140.

[15] Shuvo, M. S., Sakib, M. N., Rahman, R., & Saha, S. (2022). Particle deposition and characteristics of turbulent flow in converging and diverging nozzles using Eulerian-Lagrangian approach. Results in Engineering, 16, 100669. doi:10.1016/j.rineng.2022.100669.

[16] Urionabarrenetxea, E., Martín, J. M., Avello, A., & Rivas, A. (2022). Simulation and validation of the gas flow in close-coupled gas atomisation process: Influence of the inlet gas pressure and the throat width of the supersonic gas nozzle. Powder Technology, 407, 117688. doi:10.1016/j.powtec.2022.117688.

[17] Aniket, M., & Bhagat, D. (2022). CFD Analysis and Parameter Optimization of Convergent Divergent Nozzle. International Journal of All Research Education and Scientific Methods, 10(7), 2455–6211.

[18] Zema, T. B. (2022). A 3-D Numerical Investigation and Parametric_CFD_Analysis of Flow Through Convergent-Divergent Nozzle Using ANSYS_CFX. Journal of University of Shanghai for Science and Technology, 24, 305–314.

[19] Hua, J., Gobber, F. S., Actis Grande, M., Mortensen, D., & Odden, J. O. (2024). A numerical modeling framework for predicting the effects of operational parameters on particle size distribution in the gas atomization process for Nickel-Silicon alloys. Powder Technology, 435, 119408. doi:10.1016/j.powtec.2024.119408.

[20] Samuel J, J., Mullis, A. M., & Borman, D. J. (2024). CFD modelling of Close-Coupled Gas Atomisation (CCGA) process by employing the Euler-Lagrange approach to understand melt flow instabilities. Chemical Engineering Science, 295, 120205. doi:10.1016/j.ces.2024.120205.

[21] Wang, P., Li, X., Zhou, X., Chen, Z., Wang, M., Gan, P., Ren, X., & Yu, Z. (2024). Numerical Simulation on Metallic Droplet Deformation and Breakup Concerning Particle Morphology and Hollow Particle Formation During Gas Atomization. Transactions of Nonferrous Metals Society of China, 34(7), 2074–2094. doi:10.1016/S1003-6326(24)66526-X.

[22] Muratal, O., Yamanoğlu, R., Duran, C., Gönülalan, Y., Akyıldız, Y., Koç, F. G., & Barutçuoğlu, B. (2024). Production of Ni-Hard Alloy Powders by Gas Atomization. International Journal of 3D Printing Technologies and Digital Industry, 8(1), 124–129. doi:10.46519/ij3dptdi.1402760.

[23] Cui, C., Stern, F., Ellendt, N., Uhlenwinkel, V., Steinbacher, M., Tenkamp, J., Walther, F., & Fechte-Heinen, R. (2023). Gas Atomization of Duplex Stainless-Steel Powder for Laser Powder Bed Fusion. Materials, 16(1), 435. doi:10.3390/ma16010435.

[24] Çetin, T., Akkaş, M., & Boz, M. (2020). Investigation of the effect of gas pressure on powder characterization of AM60 magnesium alloy powder produced by gas atomization method. Journal of the Faculty of Engineering and Architecture of Gazi University, 35(2), 967–977. doi:10.17341/gazimmfd.497759.

[25] Luo, S., Ouyang, Y., Wei, Q., Lai, S., Wu, Y., Wang, H., & Wang, H. (2023). Understanding the breakup behaviors of liquid jet in gas atomization for powder production. Materials and Design, 227, 111793. doi:10.1016/j.matdes.2023.111793.

[26] Fharukh Ahmed, G. M., Alrobaian, A. A., Aabid, A., & Khan, S. A. (2018). Numerical analysis of convergent-divergent nozzle using finite element method. International Journal of Mechanical and Production Engineering Research and Development, 8(6), 373–382. doi:10.24247/ijmperddec201842.

[27] Balaji, K., & Ravichandran, M. (2016). Numerical Investigation of Flow Field in a Convergent – Divergent Nozzle using Computational Fluid Dynamic Analysis. Proceedings of ICETETS 2016, Kings College of Engineering, Thanjavur, India, 24-26 February 2016, 838-844.

[28] Khan, S. A., Ibrahim, O. M., & Aabid, A. (2021). CFD analysis of compressible flows in a convergent-divergent nozzle. Materials Today: Proceedings, 46, 2835–2842. doi:10.1016/j.matpr.2021.03.074.

[29] Shariatzadeh, O. J., Abrishamkar, A., & Jafari, A. J. (2015). Computational Modeling of a Typical Supersonic Converging-Diverging Nozzle and Validation by Real Measured Data. Journal of Clean Energy Technologies, 3(3), 220–225. doi:10.7763/jocet.2015.v3.198.

[30] Hamdan, N. S., & Kaneko, A. (2024). Effect of throat diameter on the cavitation phenomenon inside an aerated Venturi tube for microbubble production. Research Square (Preprint), 1-23. doi:10.21203/rs.3.rs-4716883/v1.

[31] Palacio, J. A., Patino, I., & Orozco, W. (2023). Influence of the ratio of nozzle inlet to nozzle throat areas on the performance of a jet pump for vacuum applications using computational fluid dynamics. AIUB Journal of Science and Engineering, 22(3), 214–222. doi:10.53799/AJSE.V22I3.489.

[32] Gonin, R., Horgue, P., Guibert, R., Fabre, D., Bourguet, R., Ammouri, F., & Vyazmina, E. (2022). A computational fluid dynamic study of the filling of a gaseous hydrogen tank under two contrasted scenarios. International Journal of Hydrogen Energy, 47(55), 23278-23292. doi:10.1016/j.ijhydene.2022.03.260.

[33] Wang, P., Liu, J., Dong, Y., Zhao, H., Pang, J., & Zhang, J. (2023). Investigation on close-coupled gas atomization for Fe-based amorphous powder production via simulation and industrial trials: Part II. Particle flight and cooling during secondary atomization. Journal of Materials Research and Technology, 26, 9480–9498. doi:10.1016/j.jmrt.2023.09.249.

[34] Schwenck, D., Ellendt, N., Fischer-Bühner, J., Hofmann, P., & Uhlenwinkel, V. (2017). A novel convergent–divergent annular nozzle design for close-coupled atomisation. Powder Metallurgy, 60(3), 198–207. doi:10.1080/00325899.2017.1291098.

[35] Kaiser, R., Li, C., Yang, S., & Lee, D. (2018). A numerical simulation study of the path-resolved breakup behaviors of molten metal in high-pressure gas atomization: With emphasis on the role of shock waves in the gas/molten metal interaction. Advanced Powder Technology, 29(3), 623–630. doi:10.1016/j.apt.2017.12.003.

[36] Wei, Y., Dong, R., Zhang, Y., & Liang, S. (2023). Study on the Interface Instability of a Shock Wave–Sub-Millimeter Liquid Droplet Interface and a Numerical Investigation of Its Breakup. Applied Sciences (Switzerland), 13(24), 13283. doi:10.3390/app132413283.

[37] Popov, V. V., Grilli, M. L., Koptyug, A., Jaworska, L., Katz-Demyanetz, A., Klobčar, D., Balos, S., Postolnyi, B. O., & Goel, S. (2021). Powder bed fusion additive manufacturing using critical raw materials: A review. Materials, 14(4), 1–37. doi:10.3390/ma14040909.

[38] Ahmed, F., Ali, U., Sarker, D., Marzbanrad, E., Choi, K., Mahmoodkhani, Y., & Toyserkani, E. (2020). Study of powder recycling and its effect on printed parts during laser powder-bed fusion of 17-4 PH stainless steel. Journal of Materials Processing Technology, 278, 116522. doi:10.1016/j.jmatprotec.2019.116522.

[39] Li, R., Kim, Y. S., Tho, H. Van, Yum, Y. J., Kim, W. J., & Yang, S. Y. (2019). Additive manufacturing (AM) of piercing punches by the PBF method of metal 3D printing using mold steel powder materials. Journal of Mechanical Science and Technology, 33(2), 809–817. doi:10.1007/s12206-019-0137-0.

[40] Gokcekaya, O., Ishimoto, T., Todo, T., Wang, P., & Nakano, T. (2021). Influence of powder characteristics on densification via crystallographic texture formation: Pure tungsten prepared by laser powder bed fusion. Additive Manufacturing Letters, 1, 100016. doi:10.1016/j.addlet.2021.100016.

[41] Ninpetch, P., Kowitwarangkul, P., Mahathanabodee, S., Chalermkarnnon, P., & Rattanadecho, P. (2021). Computational investigation of thermal behavior and molten metal flow with moving laser heat source for selective laser melting process. Case Studies in Thermal Engineering, 24, 100860. doi:10.1016/j.csite.2021.100860.

[42] Bhavar, V., Kattire, P., Patil, V., Khot, S., Gujar, K., & Singh, R. (2017). A review on powder bed fusion technology of metal additive manufacturing. Additive manufacturing handbook, 251-253. doi:10.1201/9781315119106-15.

[43] Sidambe, A. T., Tian, Y., Prangnell, P. B., & Fox, P. (2019). Effect of processing parameters on the densification, microstructure and crystallographic texture during the laser powder bed fusion of pure tungsten. International Journal of Refractory Metals and Hard Materials, 78, 254–263. doi:10.1016/j.ijrmhm.2018.10.004.

[44] Fan, Q., Li, J., Zheng, L., Hao, C., Zhang, Q., & Wang, Y. (2024). Effect of heat treatment on microstructure and mechanical properties of selective laser melted Inconel 718 alloy. PLoS ONE, 19(9 September), 309156. doi:10.1371/journal.pone.0309156.

[45] Iebba, M., Astarita, A., Mistretta, D., Colonna, I., Liberini, M., Scherillo, F., Pirozzi, C., Borrelli, R., Franchitti, S., & Squillace, A. (2017). Influence of Powder Characteristics on Formation of Porosity in Additive Manufacturing of Ti-6Al-4V Components. Journal of Materials Engineering and Performance, 26(8), 4138–4147. doi:10.1007/s11665-017-2796-2.

[46] Sofia, D., Barletta, D., & Poletto, M. (2018). Laser sintering process of ceramic powders: The effect of particle size on the mechanical properties of sintered layers. Additive Manufacturing, 23, 215–224. doi:10.1016/j.addma.2018.08.012.

[47] Zhang, S., Alavi, S., Kashani, A., Ma, Y., Zhan, Y., Dai, W., Li, W., & Mostaghimi, J. (2021). Simulation of Supersonic High-Pressure Gas Atomizer for Metal Powder Production. Journal of Thermal Spray Technology, 30(7), 1968–1994. doi:10.1007/s11666-021-01256-1.

[48] Daskiran, C., Xue, X., Cui, F., Katz, J., & Boufadel, M. C. (2021). Large eddy simulation and experiment of shear breakup in liquid-liquid jet: Formation of ligaments and droplets. International Journal of Heat and Fluid Flow, 89, 108810. doi:10.1016/j.ijheatfluidflow.2021.108810.

[49] Hanthanan Arachchilage, K., Haghshenas, M., Park, S., Zhou, L., Sohn, Y., McWilliams, B., Cho, K., & Kumar, R. (2019). Numerical simulation of high-pressure gas atomization of two-phase flow: Effect of gas pressure on droplet size distribution. Advanced Powder Technology, 30(11), 2726–2732. doi:10.1016/j.apt.2019.08.019.

[50] Gonabadi, H., Hosseini, S. F., Chen, Y., & Bull, S. (2024). Size effects of voids on the mechanical properties of 3D printed parts. International Journal of Advanced Manufacturing Technology, 132(11–12), 5439–5456. doi:10.1007/s00170-024-13683-9.

[51] Mehrabi, M., Gardy, J., Talebi, F. A., Farshchi, A., Hassanpour, A., & Bayly, A. E. (2023). An investigation of the effect of powder flowability on the powder spreading in additive manufacturing. Powder Technology, 413, 117997. doi:10.1016/j.powtec.2022.117997.

[52] Rando, P., & Ramaioli, M. (2022). Numerical simulations of sintering coupled with heat transfer and application to 3D printing. Additive Manufacturing, 50, 102567. doi:10.1016/j.addma.2021.102567.